Peer-reviewed version available at *Materials* **2018**, *11*, 1432; doi:10.3390/ma11081432

Article

Model for the correlation between anodic dissolution resistance and crystallographic texture in API 5L steels

Manuel Madrigal-Cano, Luis Hernández-Maya, José M. Hallen, Mónica Corrales-Luna, Elsa M. Arce-Estrada, Tu Le Manh *

Departamento de Ingeniería en Metalurgia y Materiales, ESIQIE-IPN, UPALM Edif. 7, Zacatenco, Ciudad de México CP 07738, México; mrmcano@hotmail.com (M.M.C.); luisgerardo.hm2016@gmail.com (L.H.M.); j_hallen@yahoo.com (J.M.H); monis_c5@hotmail.com (M.C.L.); earce@ipn.mx (E.M.A.E)
* Correspondence: letuprofesor@gmail.com (T.L.M.); Tel.: +52-55-572-96000 ext. 54205

Abstract: The present work shows a novel physical-mathematical model to estimate the average corrosion resistance index from the crystallographic texture in API 5L steels. The crystallographic texture of the studied steels was measured by means of the X-ray diffraction technique. The model, based on the symmetric spherical surface harmonics for a BCC structure, is capable of describing the anisotropy surface of anodic dissolution resistance of the crystal and establishing a straightforward relationship between crystallographic texture, surface roughness, and metal corrosion behavior. The predictions of the average corrosion resistance index made from the crystallographic texture were in good agreement with those obtained from potentiodynamic polarization curves for the investigated steels. This agreement validates the capacity of this model and opens the possibility of applying it as a novel criterion for the material selection and design stages in order to combat metal corrosion problems.

Keywords: Corrosion resistance index; anodic dissolution; crystallographic texture; pipeline steels; material selection

1. Introduction

The corrosion of metal and its alloy has been extensively studied in the literature [1,2]. The significant impact of corrosion on metallic structures in daily life and in the industry has been mainly concerned due the complex nature of the phenomenon. In this regard, the correct selection of materials could be an important tool and criteria for reducing the corrosion effect during the stage of the structure construction and design. A common way to evaluate the corrosion activity of metals is through the corrosion potential and current density (E_{corr} and j_{corr}), and Tafel slopes (b_a and b_c) by means of the polarization techniques [3-5]. However, these experimental techniques present several limitations, including blindness, workload, and time and resource wastes [6], and variations in the results due to the strong dependence on the sample surface state as well as many metallurgical variables of the material, namely chemical composition and microstructure [7-9]. In order to solve this problem, it is necessary to evaluate and quantify the corrosion resistance of the material by other means.

It is experimentally verified [9-18] that some metallurgical parameters, such as: grain size, grain boundary, and their distributions, as well as surface roughness, crystallographic planes, and grain orientations have a strong influence in the anodic dissolution of the metal. This, in fact, refers to anisotropy of corrosion, which in a crystal can be defined as the dependence of dissolution velocity of metals on the crystallographic directions [18]. Meanwhile, in a polycrystal this behavior depends

Peer-reviewed version available at *Materials* **2018**, *11*, 1432; doi:10.3390/ma11081432

on the crystallographic texture, since the texture develops in alloys and metals during their mechanical deformation, such as rolling, forging, drawing, etc. and the established preferred orientations can introduce significant changes to the material properties [19]. The significant effect of the crystallographic texture on the corrosion process has been studied in several works [20-22]. One of the typical examples is given in [22] in which they found that the formation of texture components {111}||ND fiber developed by warm rolling could reduce the susceptibility to hydrogen induced corrosion (HIC), while the closeness to the random texture and the strong {001}||ND texture have a harmful effect on the resistance of hot-rolled samples to HIC. In spite of this fact, a generalized model capable of describing the link between the crystallographic texture and corrosion behaviour of metals (anodic dissolution) has been lacking.

The first idea on the correlation between the pitting corrosion resistance and the crystallographic orientation was proposed Shahryari et al. [23] in which the susceptibility of the surface to pitting corrosion (the pitting susceptibility index) for a SS316LVM stainless steel was determined from electron back-scatter diffraction (EBSD) data through the generalized spherical harmonics. Nevertheless, this model presents several limitations, namely: it does not include the sample symmetry and only uses the steel sample with one type of texture, the number of coefficients of the harmonic function is small, and furthermore, the information obtained from EBSD is not statistically significant (in comparison with the X-ray macro-texture technique) to completely describe the dependence of crystallographic orientations on the anodic dissolution of the material. Meanwhile, in another approach, Venegas et al. [24] studied the influence of crystallographic texture, measured by X-ray diffraction, on pitting corrosion in low carbon steels. They proposed that the ratio of the volume fraction of the beneficial (high-resistance) texture fibers to volume fraction of the detrimental (low-resistance) fiber could be a good measure for the pitting susceptibility of the material. However, on the one hand, this model could not establish a direct link between the pitting corrosion and the crystallographic texture, since the beneficial/detrimental texture components and their volume fraction should be previously provided and carefully analyzed. On the other hand, the main interest of our work lies on the anisotropy of the anodic dissolution resistance of polycrystalline materials. Moreover, a property of a polycrystal must be properly determined by averaging that over the orientation distribution function (ODF) [25] rather than using the volume fraction.

Therefore, in this work, a new model is proposed, based on the idea of Sharyaria et al. [23], for the correlation between the metal surface anodic dissolution resistance and the crystallographic texture of three API 5L steels with different microstructures and textures. This proposed model allows predicting the average corrosion resistance index (CRI) of API 5L steels from the crystallographic texture information using the symmetrical spherical surface harmonics. The average CRI predictions made from X-ray texture measurements will be validated by comparing with the experimental results obtained from potentiodynanic polarization curves.

2. Materials and Methods

2.1 Materials

Three API 5L steel samples (X56, X52, and X60) extracted from out-of-service pipelines were used to explore the relationship between the crystallographic texture and the corrosion behavior. These samples were prepared on rolling plane (perpendicular to the normal direction (ND) of the sample reference system) and transverse planes (perpendicular to rolling direction (RD) and to transverse direction (TD)), and were cut in disk shape with dimensions of a 1 cm in diameter and 2.5 mm in thickness; their chemical composition can be seen elsewhere [25]. All the steel samples were mechanically prepared by grinding with SiC grit papers and polishing with colloidal silica down to 20 nm in order to obtain a flat and deformation-free surface. The microstructure study was carried out in a scanning electron microscopy SEM JEOL JSL-6300.

Peer-reviewed version available at *Materials* **2018**, *11*, 1432; doi:10.3390/ma11081432

2.2 Crystallographic Texture Measurements

The texture of the steel samples was obtained in an X-ray diffractometer Bruker D8 Advance with Cu Kα radiation, coupled with an Euler cradle. Three incomplete pole figures {011}, {002}, and {112} were measured on the rolling plane for each steel sample. These experimental pole figures were analyzed using the arbitrary defined cell (ADC) method [26] implemented in the LaboTex software to calculate the orientation distribution function (ODF). From this ODF, the inverse pole figure (IPF) of ND was determined for each steel sample.

2.3. Electrochemical Tests

The potentiodynamic polarization was performed in an EG&G-PAR potentiostat/galvanostat Model 263A, using a conventional three-electrode cell coupled to a water-jacketed to control the temperature by a circulator bath (PolyScience). The electrochemical cell was composed of a API 5L steel disk-shaped sample embedded in epoxy resin with an area of 0.7854 cm^2 as the working electrode (WE), a graphite bar as the counter electrode, and a saturated calomel electrode (SCE) as the reference electrode with a Luggin capillary leading to the surface of the WE. These experiments were performed in the same steel samples (surfaces), which were previously measured by the X-ray texture diffraction. The solution used to simulate the corrosive environment of pipelines was selected according to Espina-Hernández et al. [27]. The ion concentrations of this solution are in shown Table 1.

Table 1. Ions concentration for the solution used in this work.

Solution	Cl^- (ppm)	SO_4^{2-} (ppm)	pH
S**	290	16.8	4.35[1]

[1] adjusted using HNO_3 solution.

The potentiodynamic polarization curves were recorded, starting from -700 mV to +250 mV at a scan rate of 0.16 mVs^{-1}, after 30 minutes of immersion when the steel samples were stabilized at the open circuit potential. All the potentials reported in this work were presented versus SCE.

3. Model for Estimating the Average Corrosion Resistance Index from Crystallographic Texture

It is known that corrosion is an interfacial phenomenon [28]. For this reason, understanding the surface state and its associated properties (surface roughness, planar density) could be a good indicator of the corrosion susceptibility of a family plane {*hkl*} parallel to that metal surface, since crystalline defects can be active sites for corrosion nucleation and growth mechanism.

On the one hand, Venegas et al. [24] have shown that the resistance to the dissolution anodic ($R_{\{hkl\}}$) as a function of point density ($\rho_{\{hkl\}}$) associated with crystallographic planes {*hkl*} exposed to the surface of the metal can be determined by:

$$R_{\{hkl\}} = \frac{\rho_{\{hkl\}}}{\rho_{\{110\}}} = \frac{\sqrt{2}}{\sqrt{h^2+k^2+l^2}}, \tag{1}$$

subjected to the constrain: $h+k+l=2n$

where $\rho_{\{110\}}$ is the point density for the plane {110} for BCC structure and $\rho_{\{hkl\}}$ is the point density for the plane {*hkl*}, defined by:

$$\rho_{\{hkl\}} = \frac{2}{a_0^{\,2}\sqrt{h^2+k^2+l^2}} ?? h+k+l = \quad n, \tag{2}$$

where a_0 the lattice parameter is equal to 2.866 Å for pure BCC iron. All of them, hereafter, must satisfy the constrain $h+k+l=2n \ \forall \ n \in N$ for this kind of lattice.

On the other hand, Blonski et al. [29] found that the relationship between surface roughness (S_r) and crystallographic orientation can be given by:

Peer-reviewed version available at *Materials* **2018**, *11*, 1432; doi:10.3390/ma11081432

$$S_r = \frac{A_{2D}}{A_{Fe}} = \frac{8}{3\pi}\sqrt{h^2 + k^2 + l^2}, \tag{3}$$

$$A_{2D} = \frac{a_0^2}{2}\sqrt{h^2 + k^2 + l^2}, \tag{4}$$

$$A_{Fe} = \frac{3}{16}\pi a_0^2, \tag{5}$$

where A_{2D} is the area of the surface unit cell y A_{Fe} is cross-sectional area of Fe atom in bcc lattice. From Eq. (2) and (3), $\rho_{\{hkl\}}$ could be related to S_r by the following expression:

$$\rho_{\{hkl\}} = \frac{1}{S_r}, \tag{6}$$

Therefore, from Eq. (1) and (6) the relationship between $R_{\{hkl\}}$ and S_r can be established by the following proportionality:

$$R_{\{hkl\}} \propto \frac{1}{S_r}, \tag{7}$$

Eq. (7) means that if the crystallographic plane associated to the grain parallel to surface has less surface roughness, its resistance to the anodic dissolution is higher. Interestingly, this has been verified by Shahryari et al. [23] using the generalized spherical surface harmonics, which helps evaluate the anisotropic nature of corrosion behavior of stainless steel. Nevertheless, their approach does not consider the crystal – sample symmetry relationship. Therefore, it is more convenient to apply the function developed by Bunge [30] in which the symmetric spherical surface harmonics with cubic symmetry is given by:

$$E(h) = \sum_{l=4}^{l_{\max}} \sum_{\mu=1}^{M(l)} e_l^{\mu}\, \ddot{k}_l^{\mu}(h), \tag{8}$$

where e_l^{μ} is series of constants for various value of l, which were calculated using the least--squared-fitting method [23] in Mathematica software.

The symmetric spherical harmonic function with cubic symmetry, $\ddot{k}_l^{\mu}(h)$, in Eq. (8) can be determined by [30]:

$$\ddot{k}_l^{\mu}(h) = \ddot{k}_l^{\mu}(\phi, \beta) = \sum_{m=0}^{l} \ddot{B}_l^{m\mu}\, \bar{P}_l^{m}(\phi)\cos m\beta, \tag{9}$$

where $\ddot{B}_l^{m\mu}$ is the symmetry coefficients for cubic symmetry, $\bar{P}_l^{m}(\phi)$ is the normalized associated Legendre functions with ϕ $(0° \le \phi \le 45°)$ and $\beta(0° \le \beta \le 53°)$ in the asymmetric triangle of the cubic crystalline system, and $\mathbf{h} = \{h, k, l\}$ is the direction normal to the crystallographic plane of interest with Miller indices $\{hkl\}$.

The values of l in Eq. (8) were chosen to be up to 22 instead of 10 as proposed by Shahryari et al. [23] due to the fact that with small l order up to 10 the rate of change of the harmonic function will be so fast (Fig. 1 a–d), while with $l > 10$ it has a behavior closer to a real system (Fig. 1 e–i).

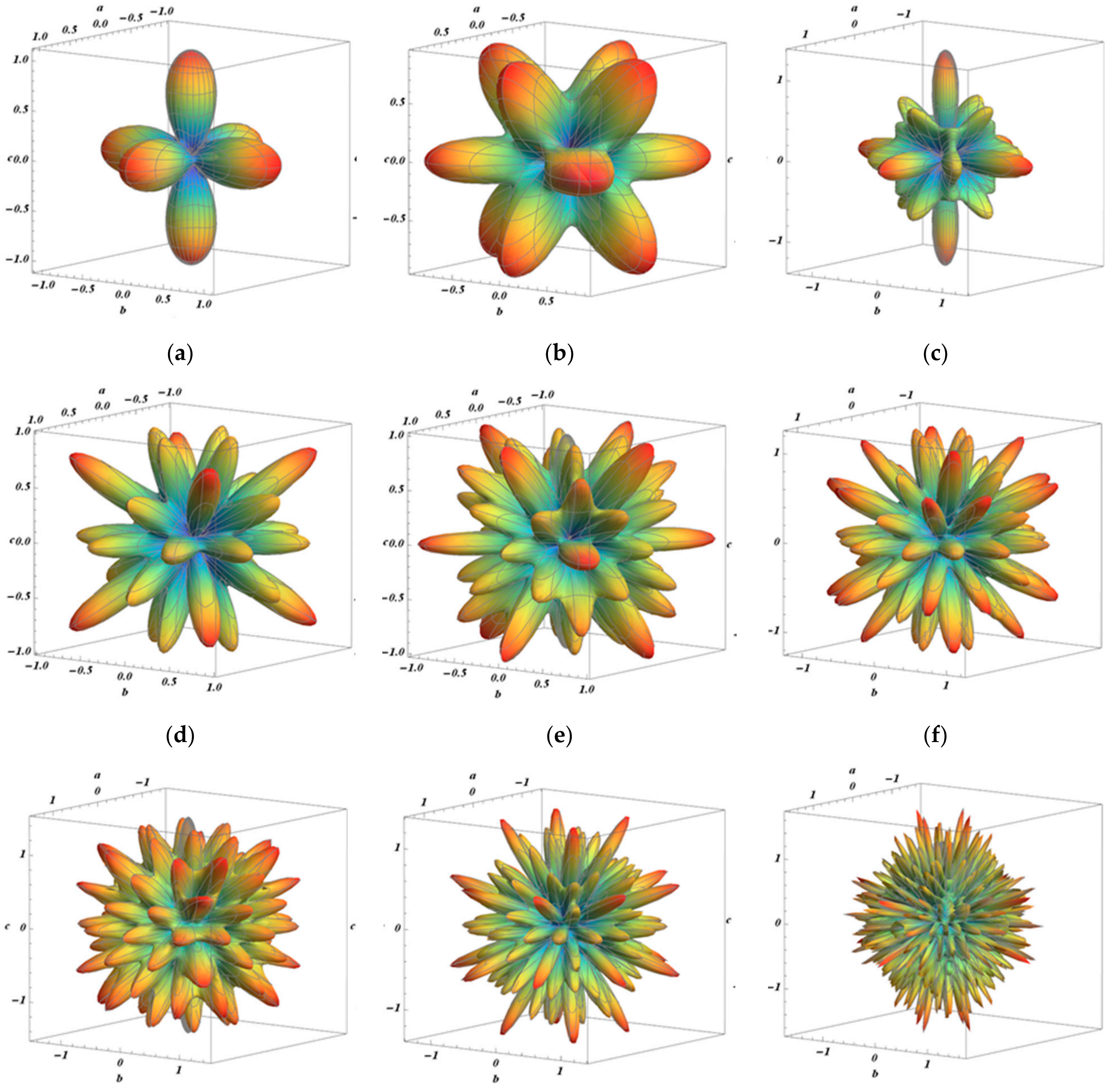

(a) (b) (c)

(d) (e) (f)

(g) (h) (i)

Figure 1. Rate of change of symmetric surface harmonics in function of the order l using Eq. (9): (a) $\boldsymbol{k}_{4}^{:1}$, (b) $\boldsymbol{k}_{6}^{:1}$, (c) $\boldsymbol{k}_{8}^{:1}$, (d) $\boldsymbol{k}_{10}^{:1}$, (e) $\boldsymbol{k}_{12}^{:2}$, (f) $\boldsymbol{k}_{14}^{:1}$, (g) $\boldsymbol{k}_{16}^{:2}$, (h) $\boldsymbol{k}_{18}^{:2}$, (i) $\boldsymbol{k}_{34}^{:1}$.

Taking into account Eq. (7) and (8), the link between the anodic dissolution resistance, *E(h)*, and surface roughness is:

$$E(h) \propto \frac{1}{S_r}, \tag{10}$$

It is important to stress that indeed Eq. (10) gives a physical meaning to the symmetric spherical surface harmonic function and possibility to describe the corrosion anisotropy in function of any crystallographic planes. Henceforth, from Eq. (10) *E(h)*, which is called CRI, can be defined as the new anisotropy function of the anodic dissolution rate for the crystallographic planes parallel to the surface, that can be estimated over the entire angular range of the asymmetric triangle of the cubic crystal system (standard triangle due to the cubic symmetry).

For a better understanding of the benefit of Eq. (10), the variation of the anodic dissolution resistance in function of the crystallographic planes, described by *E*(*h*), is represented through the inverse pole figure of the cubic crystal system, as depicted in Fig. 2. The results indicate that the tendency to suffer corrosion follow the sequence: {213} > {111} > {103} > {112} > {001} > {101}, which is in agreement with the trends observed in several works [7,8,10,11,14,15,19].

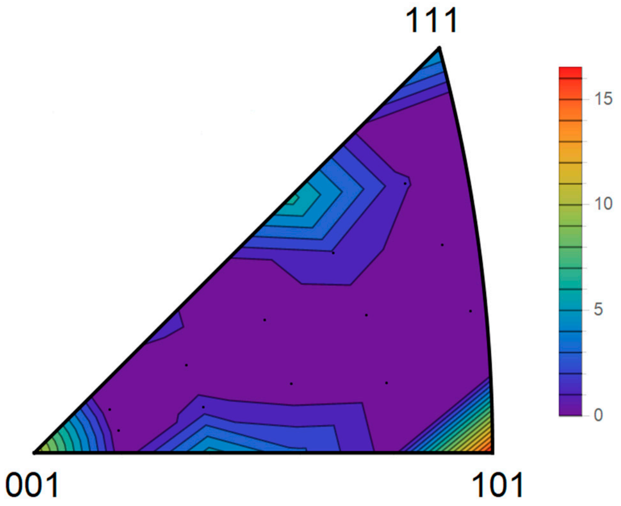

Figure 2. Anisotropy surface of anodic dissolution of BCC materials calculated for any crystallographic plane.

In order to study the corrosion property in a polycrystal, it is important to know the crystallographic texture or the distribution of crystal orientations in it. The average CRI, $\bar{E}(h)$, in a polycrystalline material with orientation distribution function (ODF), *f(g)*, can be determined for any anodic dissolution vector (Φ, β) in the sample´s reference system [30]:

$$\bar{E}(\boldsymbol{h}) = \bar{E}(\Phi,\beta) = \int_{ES} E(\Phi,\beta,g)\, f(g)\, dg\,, \tag{11}$$

where *g* is the crystal orientation and ES is the Euler space; *f(g)* should be determined considering cubic (crystal) – orthorhombic (sample) symmetry.

Since corrosion initiates on the metal surface rather than the entire volume of the material [28], the average CRI of a polycrystal is interested in the direction perpendicular to the rolling plane of the sample. Under this condition, $\bar{E}(h)$ in a polycrystal can be estimated by [23, 30]:

$$\bar{E}(h) \propto \oint\int E(\Phi,\beta)\, IPF(\Phi,\beta) \sin(\Phi)\, d\Phi d\beta\,, \tag{12}$$

where IPF(Φ, β) is the intensity of the inverse pole figure from measurement X-ray diffraction.

Eq. (12) proposes a new model for estimating the average CRI in API 5L steels from the crystallographic texture measurements. This will be evaluated in steel samples with different microstructures and textures for further comparison with results obtained from electrochemical tests.

4. Results and Discussion

4.1 Microstructure Study

Figure 3 shows the SEM micrographs represented in form of a cubic crystal for the three studied steels (X56, X52, and X60). In general, the microstructures of these steels are different (from one material to the next) and are consisted of a ferrite/pearlite structure. The equiaxial grain morphology is observed on the rolling plane with a relatively homogeneous distribution, while slightly elongated grains were observed on the transverse (RD-ND and TD-ND) planes due to the pipe manufacturing process [31-33]. Microstructural parameters, such as grain size and volume fraction of the ferrite phase, were determined by optical microscopy, as shown in Table 2. The inclusion (MnS) content in these steels is insignificant according to the work published on pipeline steels [22].

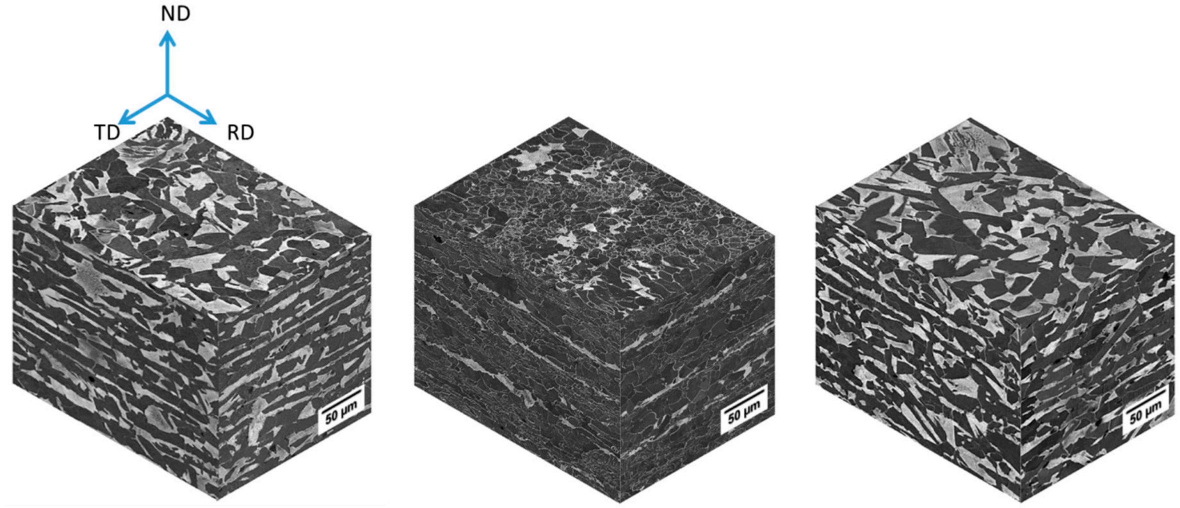

(**a**) (**b**) (**c**)

Figure 3. SEM micrographs of the studied steels: (a) X52, (b) X56, and (c) X60. The ferrite and perlite phases are represented by dark and bright colors, respectively.

Table 2. Microstructural parameters of the investigated steels.

Steels	**Average grain size (μm)**	**Ferrite content (%)**
X56	13.88 ± 0.012	75.45 ±0.05
X52	18.22 ± 0.014	64.38 ±0.03
X60	23.89 ± 0.015	65.42 ±0.03

4.2 Estimation of the Average CRI from Crystallographic Texture

Figure 4 shows the cubic-orthorhombic representation of the X-ray-derived ODF of the studied steels in the φ_2 = 45 section of Euler space [30] before electrochemical tests. It can be seen that the crystallographic texture of these steels is characterized by the presence of the {100}||ND, {111}||ND, {112}||ND, and {110}||ND texture fibers with different degrees of development [24, 32, 33]. The volume fractions ($V_{\{hkl\}}$ND) of these fibers are calculated as shown in Table 3. The formation of these fibers can be explained as the consequence of the hot rolling process during the pipe manufacturing [31-33]. X52 and X60 steels (Fig. 4b and 4c) show a texture close to random, with a relatively small degree of difference, while the X56 steel (Fig. 4a) presents a markedly strong texture dominated by {112}||ND and {111}||ND fibers. These differences in texture could influence the electrochemical behavior of these samples and consequently, their corrosion resistance.

Table 3. Volume fraction of the texture fibers (in %) of the studied steels.

Materials	**$V_{\{001\}}$ND**	**$V_{\{112\}}$ND**	**$V_{\{111\}}$ND**	**$V_{\{110\}}$ND**
X56	8.32	22.29	12.34	3.93
X52	4.57	15.14	6.51	9.36
X60	5.37	16.68	7.44	9.19

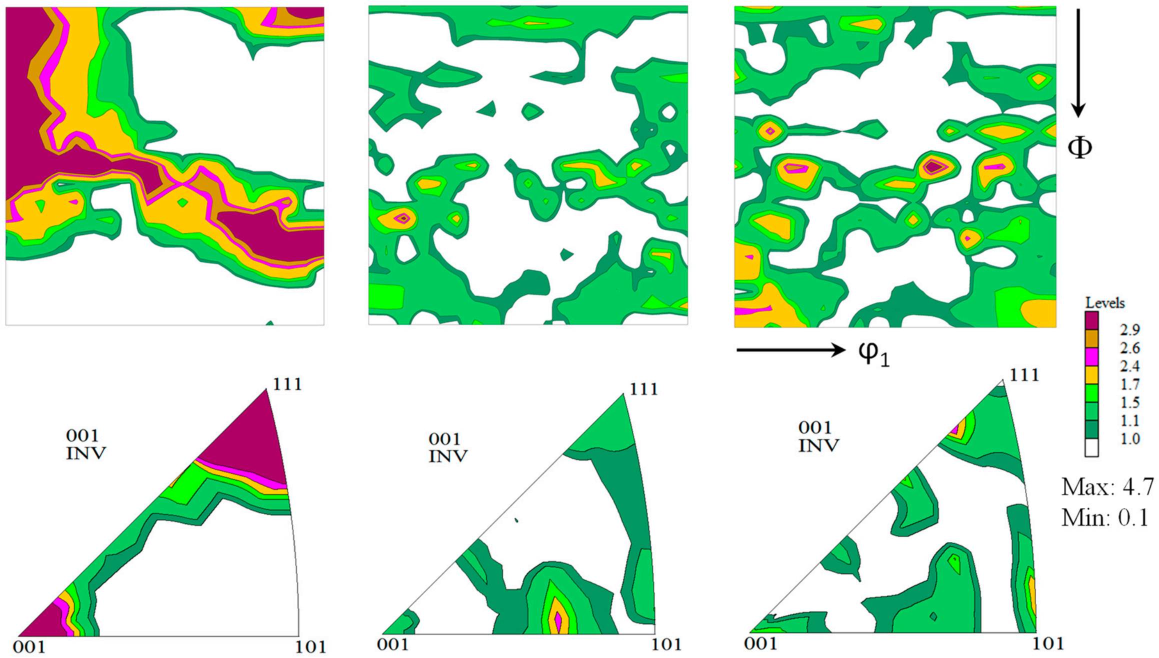

(**a**) (**b**) (**c**)

Figure 4. φ_2 = 45° section of the orthorhombic ODFs and their corresponding IPF of ND of the studied steel samples before polarization tests: (**a**) X56, (**b**) X52, (**c**) X60. The angles (Φ and φ_2) are ranging within 0 - 90° in the Euler space.

As previously explained, due to the surface behavior of corrosion phenomena it is more convenient to use data from the IPFs of ND. In fact, the representation of texture through of the IPFs is a direct way to exhibit the distribution of crystallographic planes of the grains exposed to the surface sample (crystallographic planes perpendicular to the steel sample surface). Data obtained from these IPFs were used to calculate the average CRI, $\bar{E}(h)$, which is summarized in Table 4. The results indicate that corrosion resistance of the studied steels follows the order of: X56 < X52 < X60, since the higher CRI values, the better the corrosion resistance is. According to the previous texture analysis, this order is logical, thus the high volume fraction of {112}||ND and {111}||ND fibers (see Table 3) in X56 steel clearly indicates that this material presents a more loose structure (low dense planes) than the other steels (X52 and X60) with higher volume fractions of {110}||ND fibers, since {110} are the most compact (dense) planes in BCC materials. Therefore, X56 steel may dissolve at higher rate than X52 and X60 steels. This effect can be clearly observed through the illustration of the anisotropy surface of anodic dissolution shown in Figure 2. It is important to note that this analysis only helps when texture is markedly different – in terms of both texture components and their magnitude – from one material to the next, such as X56 and X60 steel, but it is notoriously difficult when the texture is similar as can be seen in the case of X52 and X60 steels. Nevertheless, the model proposed in this paper could satisfactorily solve this problem, since Eq. (12) deals with all texture data obtained from the IPFs of the material. For the sake of validation, the average CRI predictions made from the crystallographic texture will be compared with those obtained from potentiodynamic polarization curves.

4.3 Model Validation

In order to verify the validity of the proposed model, parameters that represent the corrosion resistance of the three steels (X56, X52, and X60), were determined by the potentiodynamic polarization method and compared the predictions made from crystallographic texture measurements. It is important to stress that according to Fushimi et al. [10] the anisotropic corrosion of iron can be satisfactorily studied by means of the potentiodynamic polarization technique, as well as, it could experimentally reveal the dependence of the crystallographic orientation on corrosion resistance of the material.

Peer-reviewed version available at *Materials* **2018**, *11*, 1432; doi:10.3390/ma11081432

Figure 5 shows the comparison of the potentiodynamic polarization curves recorded onto the three steels in the solution S**. It can be observed in Fig. 5 that the three investigated steels exhibit markedly different corrosion behavior as a consequence of their difference in textures and microstructures.

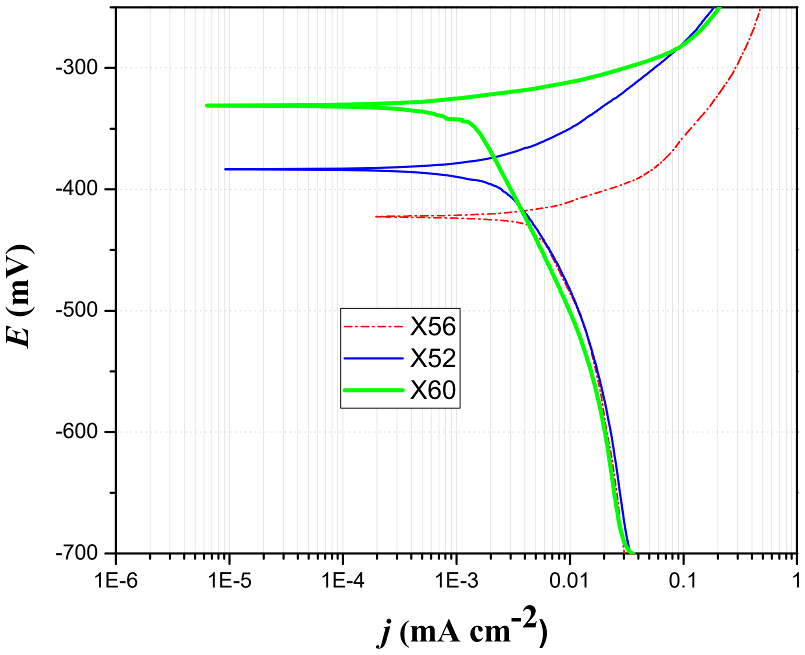

Figure 5. Potentiodynamic polarization curves of the three studied steel surfaces recorded at room temperature in the solution S**, at a scan rate of 0.16 mVs^{-1}.

From the analysis of these curves, some parameters of interest, such as: E_{corr} and corrosion current density (j_{corr}), which describe the propensity of each sample to suffer corrosion, were determined, as shown in Table 4. Also, these values can be associated with the susceptibility of the material to corrosion. Thus the less negative values of E_{corr} can be associated with the greater corrosion resistance [6]. Accordingly, the corrosion resistance should be the highest for X56 steel and the lowest for X60 steel. This corrosion resistance order agrees excellently with the CRI predictions made from crystallographic texture. However, this thermodynamic aspect would not be sufficient to predict the corrosion behavior for all materials to occur, since they have different microstructural features and textures, and a criteria regarding kinetic point of view could be appropriate satisfy the present need.

Table 4. Corrosion parameters determined from the potentiodynamic polarization curves of the studied steels.

Materials	$\overline{E}(h)$	E_{corr} **(mV)**	j_{corr} **(µA)**	b_c **(mV/dec)**
X56	6.35	427 ±8	6.19 ±0.08	177 ±9
X52	6.72	390 ±7	3.01 ±0.05	216 ±7
X60	7.01	335 ±6	1.66 ±0.03	191 ±8

In fact, this can be clarified by comparing other parameter of the corrosion process, j_{corr}, determined from the polarization curves for each steel (see Table 4). The results of Table 4 clearly indicate that X56 steel a higher j_{corr} values than those of X52 and X60 steels. In the same trend, other parameters E_{corr}, and b_c also confirm that the corrosion resistance is given by the following sequence: X56 < X52 < X60. This follows the exact order of corrosion resistance or average CRI as has been previously predicted by X-ray texture measurements using Eq. (12).

It is important to note that the grain size could be a factor that affects the corrosion behavior of the material, since X56 with the smallest grain size can be more corroded. Notwithstanding,

Peer-reviewed version available at *Materials* **2018**, *11*, 1432; doi:10.3390/ma11081432

according to Taleb et al. [28] verified that at long time exposure the effect of the grain size is negligible and in most of case on the mechanism of pitting corrosion depends strongly on the crystallographic orientation.

In general, the good agreement between average CRI predictions made from crystallographic texture and experimental results estimated from potentiodynamic polarization curves verifies the validity of the proposed and generalized model and the strong effect that the crystallographic texture has on corrosion behavior of the material. This influence can be explained due to the intimate and physical link between the surface roughness and crystallographic texture of the material. Also, it comes to support and extend the earlier idea proposed by Shahryari et al. [23] on estimating the corrosion resistance index in API 5L steels. Furthermore, the results open a new possibility to apply the proposed model as novel criteria for the selection and design of metal and its alloys, as well as an effective tool for the pipeline integrity strategy.

5. Conclusions

For the first time, a novel model is proposed and validated for the estimation of the average corrosion resistance index from the crystallographic texture in API 5L steels, with different microstructures and textures. This model is based on the symmetric spherical harmonics, considering cubic (crystal) – orthorhombic (sample) symmetry with a large number of series of constants, and capable of faithfully reproducing the anisotropic nature of corrosion behavior of the material. The strong agreement is observed between the predictions of the average corrosion resistance index made from crystallographic texture measurements and the experimental results from potentiodynamic polarization curves for all the studied steels. It is established that a material with a higher value of average corrosion resistance index could have a better corrosion resistance. The proposed and validated model provides a novel criterion for the selection and design of metal and its alloys. Furthermore, it is possible to apply as an effective tool for the pipeline integrity strategy.

Author Contributions: M.M.C. and T.L.M. developed the mathematical model and designed the experiments; J.M.H., M.M.C., M.C.L., and L.H.M. prepared the samples and performed crystallographic texture measurements; M.M.C., M.C.L. and E.M.A.E carried out electrochemical experiments. M.M.C., J.M.H. and T.L.M. analyzed and interpreted the data; M.M.C. wrote the manuscript with the assistance and revision of T.L.M., L.H.M., M.C.L., and E.M.A.E.

Funding: This research was funded by CIDIM-IPN, México, under Project 425102817 and CONACYT.

Acknowledgments: This work has been supported by CIDIM-IPN, México, under Project 425102817. The support of CONACYT is also acknowledged.

Conflicts of Interest: The authors declare no conflict of interest.

References

1. Vanaei, H.R.; Eslami, A.; Egbewande, A. A review on pipeline corrosion, in-line inspection (ILI), and corrosion growth rate models. *Int. J. Pres. Ves. Pip.* **2017**, 149, 43-54, http://dx.doi.org/10.1016/j.ijpvp.2016.11.007 (22 November 2016).
2. Tawancy, H.M.; Al-Hadhrami, L. M.; Al-Yousef, F.K. Analysis of corroded elbow section of carbon steel piping system of an oil–gas separator vessel. *Case Stud Eng. Fail Analysis* **2013,** 1, 6-14. http://dx.doi.org/10.1016/j.csefa.2012.11.001 (14 December 2012).
3. Arzaghi, E.; Abbassi, R.; Garaniya, V.; Binns, J.; Chin, C.; Khakzad, N.; Reniers, G. Developing a dynamic model for pitting and corrosion-fatigue damage of subsea pipelines. *Ocean Engineering* **2018**, 150, 391-396. https://doi.org/10.1016/j.oceaneng.2017.12.014 (16 December 2017).
4. McCafferty E. *Introduction to Corrosion Science*, Springer: New York, E.U., 2010, p.119, 978-1-4419-0454-6.
5. Bhandari, J.; Khan, F.; Abbassi, R.; Garaniya, V.; Ojeda, R. Modelling of pitting corrosion in marine and offshore steel structures - a technical review. *J. Loss Prev. Process Ind.* **2015**, 37, 39-62 DOI:10.1016/j.jlp.2015.06.008.

Peer-reviewed version available at *Materials* **2018**, *11*, 1432; doi:10.3390/ma11081432

6. Liu, A.; Ren, X.; Zhang, J.; Wang, C.; Yang, P.; Zhang, J.; An, M.; Higgins, D.; Li, Q. Wu, G. Theoretical and experimental studies of the corrosion inhibition effect of nitrotetrazolium blue chloride on copper in 0.1 M H2SO4. *RSC Adv.* **2014**, 4, 40606. DOI: 10.1039/c4ra05274a.
7. Frankel, G. S. Pitting corrosion of metals a review of critical factors, *J. Electrochem. Soc.* **1998**, 145(6), 2186-2198. DOI: 10.1149/1.1838615
8. Buck, W. R.; Leidheiser, H. The corrosion of single crystals and recrystallized single crystals of iron and steel in citric acid. *J. Electrochem. Soc.* **1957**, 104(8), 474-481. DOI: 10.1149/1.2428630.
9. Boggs, W. E.; Kachik, R. H.; Pellissier, G. E. The effects of crystallographic orientation and oxygen pressure on the oxidation of iron. *J. Electrochem. Soc.* **1967**, 114 (1), 32-39. DOI: 10.1149/1.2426502.
10. Fushimi, K.; Miyamoto, K.; Konno, H. Anisotropic corrosion of iron in pH 1 sulphuric acid. *Electrochim. Acta* **2010**, 55, 7322-7327. DOI:10.1016/j.electacta.2010.07.044 (24 July 2010).
11. Takabatake, Y.; Fushimi, K.; Nakanishi, T.; Hasegawa, Y. Grain-dependent passivation of iron in sulfuric acid solution. *J. Electrochem. Soc.* **2014**. 161(14), C594-C600. DOI: 10.1149/2.0901414jes.
12. . Wang, X.; Szpunar, J.A.; Zhang, L. Effect of surface crystallographic orientation on the oxidation behavior of Ni-based alloy. *Appl. Surf. Sci.* **2015**, 327, 532-536. http://dx.doi.org/10.1016/j.apsusc.2014.11.126 (3 December 2014).
13. Bland, L. G.; Gusieva, K.; Scully, J.R. Effect of crystallographic orientation on the corrosion of magnesium: Comparison of film forming and bare crystal facets using electrochemical impedance and Raman spectroscopy. *Electrochim. Acta* **2017**, 227, 136-151. http://dx.doi.org/10.1016/j.electacta.2016.12.107 (21 December 2016).
14. Schreiber, A.; Schultze, J. W.; Lohrengel, M.M.; Kármán, F.; Kálmán, E. Grain dependent electrochemical investigations on pure iron in acetate buffer pH 6.0. *Electrochim. Acta* **2006**, 51, 2625-2630. DOI:10.1016/j.electacta.2005.07.052.
15. Schreiber, A.; Rosenkranz, C.; Lohrengel, M. M. Grain-dependent anodic dissolution of iron. *Electrochim. Acta* **2007**, 52, 7738-7745. DOI:10.1016/j.electacta.2006.12.062.
16. Kyeong-Min, K.; Hyun-Kyu, K.; Park J. Y.; Lee, J. S.; Kim, S. G.; Kim, N. J.; Byeong-Joo, L. {100} texture evolution in bcc Fe sheets - computational design and experiments. *Acta Mater.* **2016**, 106, 106-116. http://dx.doi.org/10.1016/j.actamat.2016.01.003 (21 January 2016).
17. Brewick, P. T.; Kota, N.; Lewis, A. C.; DeGiorgi, V. G.; Geltmacher, A. B.; Qidwai, S. M. Microstructure-sensitive modeling of pitting corrosion: Effect of the crystallographic orientation. *Corros. Sci.* **2017**, 129, 54-69. http://dx.doi.org/10.1016/j.corsci.2017.09.009 (18 September 2017).
18. Brahim-Bounab, A.; Amaudrut, J. Y.; Tellier, C. R. Dissolution slowness surfaces of cubic crystals Part I. J. *Mater. Sci.* **1991**, 26, 5585-5594.
19. Dwivedi, D.; Lepkova, K.; Becker, T. Carbon steel corrosion: a review of key surface properties and characterization methods. *RSC Adv.* **2017**, 7, 4580-4610. DOI:10.1039/c6ra25094g (26 June 2018).
20. Arafin, M.A.; Szpunar, J.A. A Markov Chain–Monte Carlo model for intergranular stress corrosion crack propagation in polycrystalline materials. *Mat. Sci. Eng. A-Struct.* **2009**, 513-514, 254-266. DOI:10.1016/j.msea.2009.01.072.
21. Arafin, M.A.; Szpunar, J.A. A new understanding of intergranular stress corrosion cracking resistance of pipeline steel through grain boundary character and crystallographic texture studies. *Corros. Sci.* **2009**, 51, 119-128. DOI:10.1016/j.corsci.2008.10.006 (14 October 2008).
22. Venegas, V.; Caleyo, F.; Baudin, T.; Espina-Hernandez, J. H.; Hallen, J. M. On the role of crystallographic texture in mitigating hydrogen-induced cracking in pipeline steels. *Corros. Sci.* **2011**, 53, 4204-4212.
23. Shahryari, A.; Szpunar, J. A.; Omanovic, S. The influence of crystallographic orientation distribution on 316LVM stainless steel pitting behavior. *Corros. Sci.* **2009**, 51, 677-682. DOI:10.1016/j.corsci.2008.12.019 (27 December 2008).
24. Venegas, V.; Caleyo, F.; Vázquez, L. E.; Baudin, T.; Hallen, J. M. On the influence of crystallographic texture on pitting corrosion in pipeline steels. *Int. J. Electrochem. Sci.* **2015**, 10, 3539-3552.
25. Manh, T. L.; Caleyo, F.; Hallen, J.M.; Pérez-Benítez, J.A.; Espina-Hernández J.H. Novel method for the accurate determination of magnetocrystalline energy from Barkhausen noise in ferromagnetic materials. *Mat. Sci. Eng.* **2017**, B 225, 98-107. http://dx.doi.org/10.1016/j.mseb.2017.08.015 (24 August 2017).
26. Pawlik, K. Determination of the orientation distribution function from pole figures in arbitrarily defined Cells. *Phys. Stat. Sol (b)*. **1986**, 134, 477.

27. Espina-Hernández, J.H.; Caleyo, F.; Venegas, V.; Hallen, J.M. Pitting corrosion in low carbon steel influenced by remanent magnetization. *Corros. Sci.* **2011**, 53, 3100-3107. DOI:10.1016/j.corsci.2011.05.044 (18 May 2011).
28. Taleb, A.; Stafiej, J. Numerical simulation of the effect of grain size on corrosion processes: Surface roughness oscillation and cluster detachment. *Corros. Sci.* **2011**, 53, 2508-2513. DOI:10.1016/j.corsci.2011.04.008 (19 April 2011).
29. Blonski, P.; Kiejna, A. Structural, electronic, and magnetic properties of bcc iron surfaces. *Surf. Sci.* **2007**, 601, 123-133.
30. Bunge, H. J.; *Texture Analysis in Materials Science, Mathematical Methods*, British Library Cataloguing in Publication Data: Belin, Germany 1982, p.351-377;0-408-10642-5.
31. Raabe, D.; Lucke, K. Texture and microstructure of hot rolled steel. *Scr. Mater.* **1992**, 26, 1221-1226.
32. Manh, T. L.; Caleyo, F.; Hallen, J.M.; Espina-Hernández, J.H.; Pérez-Benitez, J.A. Model for the correlation between magnetocrystalline energy and Barkhausen noise in ferromagnetic materials. *J. Magn. Magn. Mater.* **2018**, 454, 155-164. https://doi.org/10.1016/j.jmmm.2018.01.066.
33. Manh, T. L.; Hallen, J.M.; Caleyo, F.; Sierra-Marquez, A.L. Electron backscatter diffraction helps direct calculation of magnetocrystalline anisotropy energy in API 5L steels. *Mater. Charact.* **2018**, 141, 86 -96. https://doi.org/10.1016/j.matchar.2018.04.033 (24 April 2018).